Environ. Eng. Res. 2024; 29(4): 230596
https://doi.org/10.4491/eer.2023.596

pISSN 1226-1025
eISSN 2005-968X

Research

Visible light-driven photocatalytic degradation of doxycycline using ZnO/g-C_3N_4/biochar composite in aqueous solution

Nguyen Van Hung[1†], Bui Thi Minh Nguyet[1*], Nguyen Huu Nghi[1*], Nguyen Minh Luon[1*], Nguyen Ngoc Bich[1*], Le Van Thanh Son[2*], Nguyen Trung Kien[3*], Dao Ngoc Nhiem[3*], Nguyen Thanh Tuoi[4*], Dinh Quang Khieu[4††*]

[1]*Faculty of Natural Sciences and Education, Dong Thap University, 870000, Vietnam*
[2]*University of Education and Science, The University of Danang, 550000, Vietnam*
[3]*Institute of Materials Science, VAST, 100000, Vietnam*
[4]*University of Sciences, Hue University, Hue, 530000, Vietnam*
**These authors contributed equally to this work*

Received September 29, 2023 **Revised** December 19, 2023 **Accepted** December 27, 2023

ABSTRACT

In the present work, ZnO/*g*-C_3N_4/biochar was prepared, and it was used for visible-light driven photocatalytic degradation of some colorants (methylene blue, rhodamine B, methyl orange) and some antibiotics (doxycycline, ciprofloxacin, amoxicilline). Biochar was prepared by pyrolysing *Phragmites australis* biomass. The ZnO/*g*-C_3N_4/biochar composite was synthesized with the alkaline hydrolysis method. The obtained materials were characterized by X-ray diffraction, scanning electron microscopy, transition electron microscopy, energy dispersive X-ray/elemental mapping, ultraviolet-visible-diffuse reflectance spectroscopy, photoluminescence spectroscopy, nitrogen adsorption/desorption isotherms and X-ray photoelectron spectroscopy. The results show that ZnO nanoparticles with a large surface area are highly dispersed on the *g*-C_3N_4 particle surface and biochar. The composite exhibits superior photocatalytic degradation ability toward doxycycline, a broad-spectrum antibiotic of the tetracycline compared with individual components (ZnO or *g*-C_3N_4) and satisfies stability after six treatment cycles. The kinetics and degradation mechanisms of doxycyline were also addressed. In addition, the present catalyst also exhibits the photocatalytic degradation of methylene blue, rhodamine B, methyl orange, ciprofloxacin and amoxicillin in visible-light regions.

Keywords: Biochar, Doxycycline, *g*-C_3N_4, Photocatalytic degradation, ZnO

Graphical Abstract

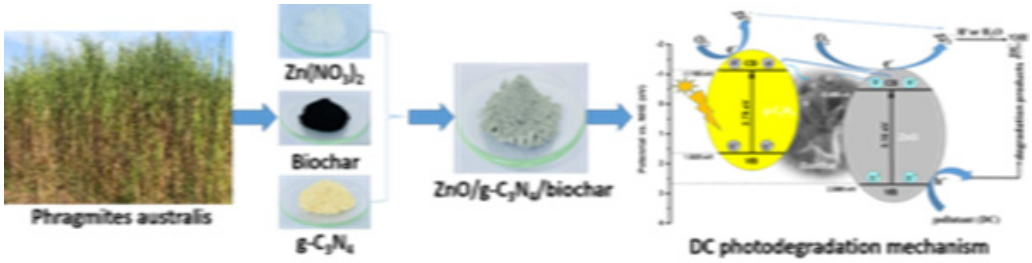

† Corresponding author
E-mail: nguyenvanhung@dthu.edu.vn (N.V.H.), dqkhieu@hueuni.edu.vn (D.Q.K.)
Tel: +84 988449905 (N.V.H.), +84 368706850 (D.Q.K.)
ORCID: 0000-0002-7184-0715 (N.V.H.), 0000-0003-3473-6377 (D.Q.K.)

1. Introduction

Antibiotics are widely utilized for human and veterinary disease treatments, and they are present in various domestic wastewater sources, from hospitals to livestock farms [1]. During use, only a part of the antibiotics is absorbed and metabolized in the human/animal body, and most of them are excreted unchanged. Numerous antibiotics are stable and do not decompose naturally, and their residues left in wastewater and sludge can be dispersed to receiving sources and accumulate in the ecosystems, increasing the risk of antibiotic-resistance genes in livestock and humans [2]. Doxycycline (DC, $C_{22}H_{24}N_2O_8$) is a broad-spectrum antibiotic of the tetracycline class, used in the treatment of infections caused by bacteria and certain parasites in humans and animals [3, 4]. Because of its antibacterial properties, even at low concentrations, doxycycline can induce antibiotic resistance to microorganisms, altering the microbial structure and function and posing a serious risk to humans and animals [4, 5]. Since contaminated wastewater is a major source of antibiotics, the development of effective wastewater treatment methods is necessary to remove these harmful compounds [5, 6]. Up to the present, numerous methods, such as biodegradation, electrochemistry, flocculation, and membrane filter, are used to treat antibiotics [2, 7]. However, the complex and persistent structure of antibiotics, the formation of toxic by-products, and high operating or maintenance costs make these methods less effective. Photocatalytic oxidation is currently considered as one of the effective technique in wastewater treatment, especially for wastewater containing toxic and persistent organic pollutants that are not easily degraded and removed with biological or other traditional methods [8, 9]. Photocatalytic processes can completely decompose organic pollutants *via* the formation of hydroxyl and superoxide radicals that produce less toxic compounds without generating sludge [10, 11].

Although TiO_2 photocatalysts have been widely used for environmental applications, zinc oxide (ZnO), a semiconductor, is found to be an ideal material to replace TiO_2 because of its unique properties, such as low cost, sustainability, versatile applications, and high photocatalytic activity [11, 12]. However, pristine ZnO has a large energy bandgap (about 3.37 eV), which is only excited in the ultraviolet-light region, thus limiting its ability to work under sunlight conditions [12]. To overcome these limitations, various techniques related to the modification of ZnO have been developed, such as morphology and composition control [13, 14], metal ion doping [15, 16], and non-metal ion doping [17, 18] coupled with other photocatalysts [19].

Graphitic carbon nitride (g-C_3N_4), a non-metallic polymer semiconductor, is suitable for combining with ZnO because of its narrow band gap (2.7 eV) [20]. Numerous studies show that ZnO/g-C_3N_4 heterojunction coupling can promote the separation of electron-hole pairs, thus improving the photocatalytic degradation efficiency [21, 22]. Kuang *et al.* reported that the heterojunction not only increases the separation efficiency of the photogenerated electron-hole pairs but also provides a long shift of the optical absorption to the visible light region [23]. They coated the surface of ZnO nanotubes with a g-C_3N_4 layer of 20-30 nm thickness. As a result, the g-C_3N_4/ZnO materials have significantly higher photodegradability for methylene blue under visible light than individual components (g-C_3N_4 or ZnO) [23]. To further enhance the photocatalytic activity of ZnO/g-C_3N_4 materials and expand the application range of this material, researchers have studied immobilizing them on different substrates such as outer non-woven layer [24], $NiFe_2O_4$ [25], perlite [26], stainless steel mesh [27], and graphene oxide [28].

Biochar is super charcoal fabricated by calcining any biomass, such as rice husk, corncob, husk or stalk, potato or soy or wheat straw, without oxygen [29, 30]. *Phragmites australis*, a common reed, is a vigorous and aggressive species. It grows at rivers, the upper edges of estuaries, streams and other wetlands. *Phragmites australis* stems are composed of tissues with porous structure, which is an ideal biomass source to form porous biochar [31]. Biochar is a promising material in environmental remediation thanks to its excellent physicochemical properties, such as large surface area, large pore diameter, and numerous active functional groups on the surface. Besides its superior adsorption capacity, biochar can act as an electron acceptor and participate in electron transport. In addition, its significant stability allows biochar to be an excellent support for photocatalysts [32]. In recent years, biochar-based materials, such as ZnO/biochar [33], TiO_2/biochar [34], Co_3O_4/biochar [35], CuO/biochar [36], and BiOBr/biochar [37], have been used as photocatalysts for the decomposition of various pollutants. However, to our best knowledge, there is a lack of research on loading ZnO/g-C_3N_4 on biochar matrix.

In this work, biochar was fabricated from *Phragmites australis* stems. The ZnO/g-C_3N_4 loaded biochar photocatalysts (ZnO/g-C_3N_4/biochar) were synthesized via a simple alkaline hydrolysis method. The photocatalytic activity of the photocatalysts was evaluated based on the photodegradation of doxycycline under visible-light ($\lambda > 420$ nm) irradiation.

2. Materials and Methods

2.1 Materials

Phragmites australis samples were collected from a wetland in Dong Thap province, Vietnam, and cleaned with tap water to remove dirt and other impurities adhered to their surfaces. The stems were dried under sunlight for four days before being finely ground to approximately 1-2 mm sizes. The obtained biomass was rinsed with water and dried in a vacuum oven at 70℃ to get a constant weight. The product was stored in a desiccator and used as raw *P. australis* biomass (cellulose 43.31%, hemicellulose 30.82%, and lignin 20.37%) [38].

Sodium hydroxide (NaOH, ≥99%), hydrochloric acid (HCl, 37%), potassium iodide (KI, ≥99.5%), potassium bromate ($KBrO_3$, 99.8%), urea ($CO(NH_2)_2$, >99%), and sodium chloride (NaCl, ≥99.5%) were purchased from Merck. Zinc nitrate hexahydrate ($Zn(NO_3)_2{\cdot}6H_2O$, ≥99.0%), *tert*-butanol ($(CH_3)_3COH$, tBA, 99.5%), doxycycline hyclate ($C_{22}H_{24}N_2O_8{\cdot}HCl{\cdot}0.5H_2O{\cdot}0.5C_2H_6O$, DC, 93.5% (HPLC)) and L-ascorbic acid ($C_6H_8O_6$, AA, 99%) were obtained from Sigma – Aldrich. All chemicals used were of analytical grade and were used as received without any further purification.

2.2. Methods

2.2.1. Synthesis of ZnO/g-C_3N_4/biochar

Add 3.0 g of raw *P. australis* biomass to a porcelain boat and calcinate it under N_2 atmosphere at 400℃ for 2 h (heating rate 3℃·min^{-1}). The product was first washed with 1 M HCl solution and then with distilled water several times until the filtrate was neutral. The washed product was dried at 105℃ to constant weight and stored in a desiccator to obtain biochar for further use.

5.0 g of urea was placed in a porcelain boat, wrapped in aluminum foil and calcined in an N_2 atmosphere at 520℃ for 2 h (heating rate 3℃·min^{-1}). The obtained yellow powder was placed in a beaker containing distilled water and sonicated for 30 min. The solid was then filtered and dried at 105℃ for 12 h, yielding pristine g-C_3N_4.

In the present work, the ZnO/g-C_3N_4 with the ratio of ZnO to g-C_3N_4 (2.0/1.0 in weight) were mixed with biochar according to different ratios. Briefly, dissolve 7.437 g of zinc nitrate hexahydrate in a 250 mL beaker containing 80 mL of distilled water. Add a certain amount of biochar (0.25; 0.50; 0.75 and 1.00 g) and 1.0 g of g-C_3N_4 to the zinc nitrate solution and stir the obtained mixture for 12 h. Next, slowly add 50 mL of a 1 M NaOH solution dropwise, hydrolyse the mixture at ambient temperature for 4 h, and let the mixture stand for 1 h. Then, the mixture was filtered and washed with distilled water until the filtrate became neutral. After washing, the product was dried at 105℃ for 12 h (heating rate 3℃·min^{-1}), then finely ground and calcined in the N_2 atmosphere at 450℃ for 2 h to obtain the ZnO/g-C_3N_4/biochar composites. The final products were calculated so that the theoretical mass ratios of ZnO/g-C_3N_4/biochar correspond to 2/1.0/0.25 (ZCNB-0.25); 2/1.0/0.50 (ZCNB-0.50); 2/1.0/0.75 (ZCNB-0.75) and 2/1.0/1.00 (ZCNB-1.00). The photocatalytic activity of ZCNB with different mass ratios was tested toward DC degradation (Table S1). Since the sample of ZCNB-0.50 exhibited the highest DC degradation the samples with similar compositions of ZCNB-0.50 synthesized were calcined at different temperatures of 400; 450; 500; 550 and 600℃ for 2 hours. Its photocatalytic activity toward DC degradation was presented in Table S2. It was found that the sample calcined at 450℃ for 2 hours was able to achieve the highest catalytic activity. Therefore, this sample was selected for further experiments. For the sake of comparison, ZnO/g-C_3N_4 (ZCN) was synthesised under the same conditions without biochar.

2.2.2. Material Characterization

X-ray diffraction (XRD) patterns were recorded on a Bruker D8 Advance X-ray diffractometer (Bruker, Germany) with an operating voltage of 40 kV, a current of 40 mA, and a CuKα radiation source, and λ = 0.15401 nm. The transmission electron microscopy (TEM) and scanning electron microscopy (SEM) images were obtained with a JEOL JEM-1010 and a FEI Nova NanoSEM 450, respectively. The elemental analysis was conducted by using EDX mapping spectroscopy on a TEAM Apollo XL EDS machine. Fourier transform-infrared (FT-IR) spectra of the samples were recorded on an IR Affinity-1S spectrophotometer (Shimadzu). Ultraviolet- visible-diffuse reflectance (UV-Vis-DRS) spectra were obtained with the UV-2600 (Shimadzu) instrument. The nitrogen adsorption/desorption isotherms were determined by using a Quantachrome TriStar 3000 V6.07A adsorption instrument. The photoluminescence (PL) spectra were recorded by using a Horiba Fluorolog 3 FL3-22 with the excitation light at 370 nm. X-ray photoelectron spectra (XPS) were recorded by ESCA-3400 (Shimadzu) with Mg Kα (1253.6 eV, 10 kV, 20 mA). Binding energy was corrected using peak Au 4f7/2 (powder) at 84.0 eV. Ultraviolet-visible (UV-Vis) spectra were obtained by a UV-Vis spectrophotometer (Spectro UV-2650, Labomed-USA).

2.2.3. Photocatalytic Degradation of Doxycycline

First, 0.1 g of catalyst was added to a 500-mL beaker containing 200 mL of an aqueous suspension of 25 mg·L^{-1} DC. Then, a light source (50 W, 220 V Compact lamps (Dien Quang)) equipped with a wavelength cut-off filter (λ ≤ 420 nm, d = 77 mm) was applied to the mixture. Before illumination, the suspension was stirred magnetically in the dark for 60 min to ensure adsorption/desorption equilibrium. A 5 mL of the suspension was withdrawn at a specified time and centrifuged to remove the solid catalyst. Finally, the concentration of DC in the supernatant was determined with a UV-Vis spectrophotometer (Spectro UV-2650, Labomed, USA) at the maximum wavelength of 346 nm [39]. The adsorption efficiency (AE) of DC was calculated according to Eq. (1):

$$\text{AE}\ (\%) = 100 \times (C_0 - C_{0e})/C_0 \quad (1)$$

where C_0 (mg·L^{-1}) is the initial concentration of DC, and C_{0e} (mg·L^{-1}) is the concentration of DC at sorption equilibrium time t (min).

The photodegradation efficiency (PE) of the photocatalyst was calculated according to Eq. (2):

$$\text{PE}\ (\%) = 100 \times (C_{0e} - C_t)/C_{0e} \quad (2)$$

where C_{0e} and C_t (mg·L^{-1}) are the DC concentration at sorption equilibrium and at irradiated time of t (min). According to the Langmuir-Hinshelwood kinetics model, the photocatalytic degradation of DC can be described according to the apparent pseudo-first-order kinetic equation [40, 41]:

$$\ln\frac{C_t}{C_{0e}} = -k \times t \quad (3)$$

where k is the apparent *pseudo*-first-order rate constant; C_{0e} and C_t (mg·L^{-1}) are the DC concentrations at equilibrium and at irradiated time of t (min).

3. Results and Discussion

3.1. Characterization of Photocatalysts

XRD patterns of ZnO, g-C_3N_4, biochar, ZCN, and ZCNB are shown in Fig. 1a. We can see that the XRD pattern of biochar has almost no diffraction peaks because of its amorphous structure [42]. The XRD pattern of ZnO presents characteristic diffraction peaks of the ZnO hexagonal wurtzite-phase structure at 2θ angles of 31.7, 34.4, 36.2, 47.5, 56.6, 62.8, 66.4, 67.9, 69.1, 72.6, and 76.9°, indexed as (100), (002), (101), (102), (110), (103), (200), (112), (201), (004), and (202) planes, respectively (JCPDS-01-075-9743). As for g-C_3N_4,

the diffraction characteristic peaks at 13.1 and 27.4° are attributed to the (100) and (002) planes, as reported previously [43-45]. The ZCN sample also shows characteristic diffraction peaks for the ZnO wurtzite structure, but their intensity is lower than that of pristine ZnO. This decrease indicates the formation of g-C_3N_4/ZnO composite, and it is possible that g-C_3N_4 inhibits ZnO crystal growth, as reported in previous works [22, 46]. Similar to g-C_3N_4, ZCNB exhibits a new phase of zinc cyanamide (ZnNCN) with low diffraction intensity at 2θ angles of approximately 19.1, 27.9, and 28.6° for faces (101), (211) and (220), respectively, besides the characteristic diffraction peaks of ZnO [47]. This structure might result from condensation between the amino triazine group and the surface hydroxyl groups of ZnO to form Zn-N bonds [48].

The average crystal size of the ZnO, ZCNB, and ZCNB samples is about 30.3, 26.6, and 25.7 nm, according to the Scherrer equation at the diffraction peak (101), respectively (Table S3). The variation in grain size indicates that g-C_3N_4 and biochar can significantly inhibit the crystal growth of ZnO in the composites.

The functional groups of ZnO, g-C_3N_4, biochar, ZCN, and ZCNB are assessed via the FTIR spectroscopic spectra (Fig. 1b). We can see that all samples have absorption bands at around 3400 cm^{-1} and 2350 cm^{-1}, related to the stretching vibrations of O–H in water and C–C in biochar, oxygen in the carbon dioxide molecule is adsorbed on the sample surface [21]. The absorption bands of ZnO observed at around 3400 cm^{-1}, 1640 cm^{-1}, and 498 cm^{-1} are related to the –OH, H–O–H and Zn–O stretching vibrations, respectively [48, 49]. For biochar, in addition to the absorption bands related to the –OH and C–O vibrations as mentioned above, there are also absorption bands at 2924 cm^{-1} and 1619 cm^{-1}, assigned to asymmetry vibrations of C–H and sp^2 character of C=C [37, 49]. The band at 1462 cm^{-1} can be attributed to the stretching vibration of –COO– [50]. The region between 900–1300 cm^{-1} and 1385 cm^{-1} is thought to be involved with C–O vibration and the binding vibrations of O–H, C–C, and C–H [51, 52]. For g-C_3N_4, the wide absorption region between 3200 cm^{-1} and 3600 cm^{-1} is thought to be responsible for the stretching vibrations of N–H and O–H [49]. Furthermore, sample g-C_3N_4 has several typical bands for the stretching vibrations of the C–N heterojunctions

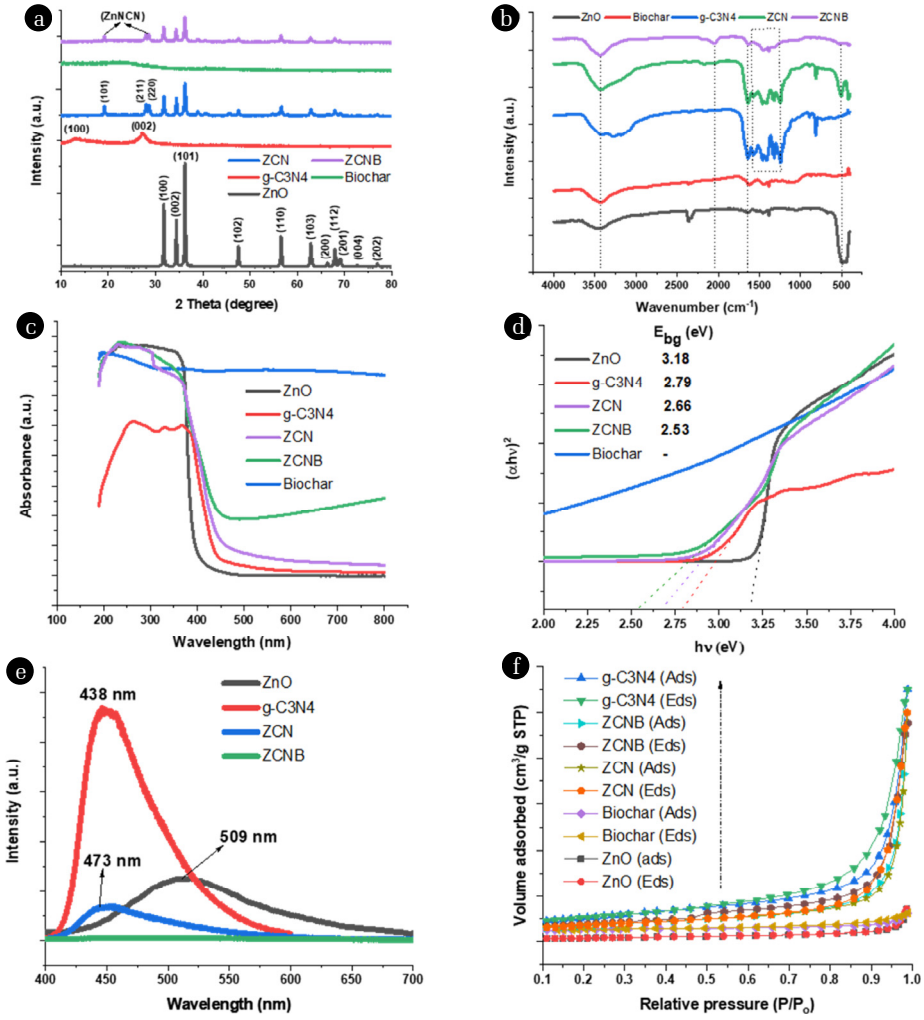

Fig. 1. The XRD patterns (a), FTIR spectra (b), UV-Vis DR spectra (c), Tauc's plots (d), PL spectra (e), N_2 sorption/desorption isotherms of ZnO, g-C_3N_4, biochar, ZCN, and ZCNB (f).

(1636 cm^{-1}, 1459 cm^{-1}, and 1410 cm^{-1}) and high-intensity strain vibrations of tri-unit s-triazine at 813 cm^{-1} [44, 48]. The bands at 1317 cm^{-1} and 1240 cm^{-1} are associated with aromatic C–N stretching [44, 48]. More importantly, the absence of absorption bands at 3000 cm^{-1} and 2200 cm^{-1} rules out the –C≡C– bond formation. The ZCN and ZCNB samples also have characteristic bands but with a lower intensity than that of the component materials, demonstrating the successful formation of heterojunction in the composite [22, 53]. In addition, from Fig. 1b, we also observe that both ZCN and ZCNB composite samples have a new absorption band at 2050 cm^{-1}, which is typical for the asymmetric stretching vibration of −N=C=N− [54], and this is also consistent with the XRD analysis. Xie et al. suggest that the formation of the g-C_3N_4/ZnNCN heterostructure can enhance the separation efficiency between photogenerated electrons and holes [54], which is one of the crucial factors for improving the photocatalytic activity of photocatalysts. It is possible that g-C_3N_4 uniformly coats ZnO nanoparticles, leading to blocking the order stacking pattern of g-C_3N_4 in the long-range order [20, 21].

The optical properties of ZnO, g-C_3N_4, biochar, ZCN, and ZCNB are estimated by using UV-Vis absorption spectroscopy. The absorption spectra exhibit the adsorption band covering the ultraviolet visible light region (Fig. 1c) [55]. It can be seen that the pristine ZnO has an upward-moving optical absorption edge at a wavelength of about 390 nm. The g-C_3N_4 sample has an upward-moving optical absorption edge in the wavelength region of about 445 nm. After the surface of g-C_3N_4 or both g-C_3N_4 and biochar was coated with ZnO, the optical absorption edge of the two composites ZCN and ZCNB has a significant blue shift towards the wavelength regions of 466 nm and 490 nm. This shift indicates a small crystal size of the ZCN and ZCNB nanocomposites. To calculate the band gap values, we use the Tauc plot relation [56].

$$\alpha \times h \times \nu = A \times (h \times \nu - E_{bg})^2 \quad (4)$$

where α is the absorption coefficient; h is the Planck constant; ν is the wavenumber; A is a constant, and E_{bg} is the energy band gap. The bandgap energy value from the absorption data was calculated by plotting $(\alpha \times h \times \nu)^2$ against the photon energy ($E_{bg} = h \times \nu$) (Fig. 1d) [22, 56]. Accordingly, the E_{bg} values of ZnO, g-C_3N_4, ZCN, and ZCNB are 3.18, 2.79, 2.66, and 2.53 eV, respectively (Table S3). Thus, a transition to lower energy occurs for the ZCNB nanocomposite, and its ability to absorb visible light increases [53].

Fig. 1e presents PL spectra of the obtained materials. The photoluminescence of ZnO, g-C_3N_4 and ZCN peak at 509; 438 and 473 nm, respectively. Since the PL intensity of g-C_3N_4 is significantly larger than that of ZnO, hence the photoluminescence of ZCN is determined by g-C_3N_4 and peaks at around 473 nm. The PL intensity of the ZCN composite is lower than that of the ZnO and g-C_3N_4 components, suggesting that g-C_3N_4 on the ZnO surface can inhibit electron-hole recombination [22]. The ZCNB composite exhibits a much lower absorption intensity than the others, indicating that the combination of ZnO with both g-C_3N_4 and biochar can enhance the separation efficiency of the photogenerated electron-hole pairs [53, 57].

The textural properties of the ZnO, g-C_3N_4, biochar, ZCN, and ZCNB samples were studied from the nitrogen adsorption/desorption isotherms at 77 K (Fig. 1f and Table S4). Their N_2 isotherms belong to type IV with an H3 hysteresis loop, according to the International Union of Pure and Applied Chemistry (IUPAC), and they indicate that the obtained samples possess a mesoporous structure [58, 59]. The H3 hysteresis loop is assigned to the non-rigid materials with plate-like particles, forming slit-shaped pores [60]. The individual components of the composite have a specific surface area (S_{BET}) as follows: 5.5 $m^2 \cdot g^{-1}$ for ZnO, 22.8 $m^2 \cdot g^{-1}$ for biochar, and 36.8 $m^2 \cdot g^{-1}$ for g-C_3N_4 (Table S2). Meanwhile, their two- and three-component composites exhibit a higher specific surface area: 28.4 $m^2 \cdot g^{-1}$ for ZCN and 25.1 $m^2 \cdot g^{-1}$ for ZCNB. These values demonstrate that g-C_3N_4 and biochar significantly improve the surface characteristics of ZnO, and the resulting composites have a capillary structure. Therefore, it can be concluded that the dispersion of ZnO onto g-C_3N_4 and biochar increases the surface area, which is beneficial for the surface reactions of the adsorbents. In general, an increased specific surface area can provide more potential active sites. Therefore, the large surface area, volume, and pore diameter of ZCNB could be one of the reasons for higher catalytic activity since the large surface area helps to increase the mass transfer rate, leading to an improved photocatalytic activity [61]. Furthermore, g-C_3N_4 in the composite not only enhances the surface area and reduces the particle size of ZnO but also forms heterojunctions. This structure is beneficial for improving the efficiency of migration of the photogenic charged particles, providing more photocatalytic sites and further improves the photodegradation efficiency [58].

The morphology of the ZnO, g-C_3N_4, biochar, ZCN, and ZCNB samples can be seen on SEM and TEM images. Fig. 2a and 2b show that ZnO exists as agglomerated spherical particles with an average diameter of about 30–35 nm. Fig. 2c displays the structure of g-C_3N_4 as thin flake-like particles with diameters ranging from a few hundred nanometres to several micrometres, overlapping the slits. Fig. 2d shows the structure of biochar in the plate form with a smooth surface. Fig. 2e and 2f display the SEM and TEM images of the ZCN composite and indicate that this material exists in the form of spherical particles with a ZnO particle size of about 30–35 nm. Fig. 2g and 2h show the SEM and TEM images of the ZCNB composite and reveal that ZCNB consists of both nodular and plate-shaped particles with a ZnO grain size of about 20–30 nm. The grains are more even than those of ZnO itself, and they seem to be successfully attached to g-C_3N_4 and biochar surfaces. Finally, Fig. 2i shows a high-resolution TEM (HRTEM) with lattice fringes with distances d(002) (2.6 Å) and d(101) (2.4 Å) for the ZnO wurtzite in ZCNB composite [62, 63].

The EDX elemental mapping of a selected area on the ZCNB composite sample is shown in Fig. 3. Carbon and nitrogen are densely distributed in the ZCNB lattice (Fig. 3d and 3e). Meanwhile, O and Zn are uniformly distributed on the surface of g-C_3N_4 and biochar in the ZCNB composite (Fig. 3f and 3g). The existence of C, N, O, and Zn on ZCNB and the merged image of C, N, O, and Zn (Fig. 3c) confirm the spatial distribution of the elements in the ZCNB composite structure. The EDX analysis further indicates the presence of C, N, O, and Zn in ZCNB (Fig. 3b). The atomic composition of the surface is as follows: C 29.17, N 36.69,

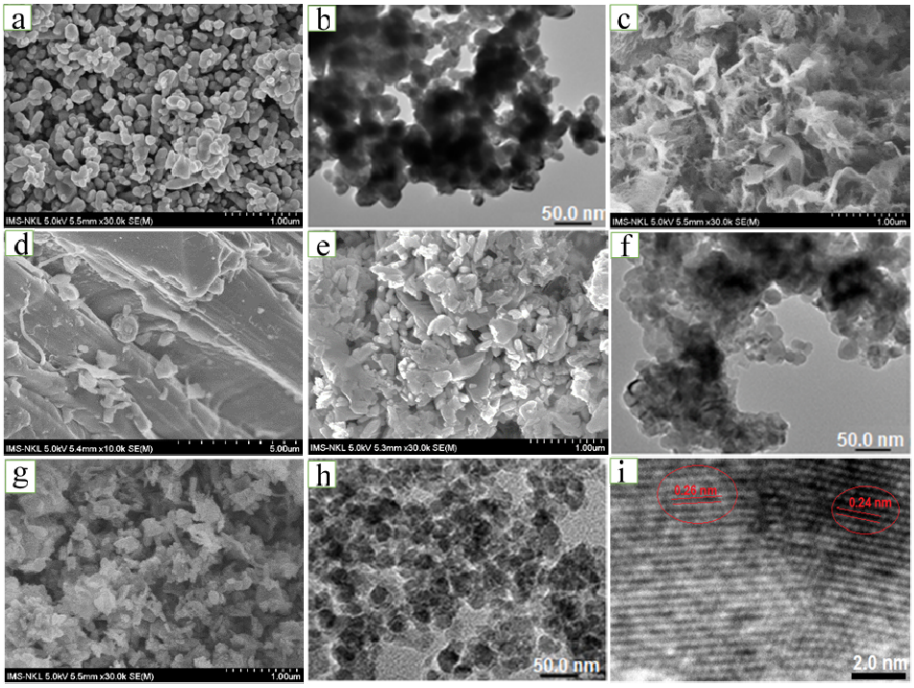

Fig. 2. SEM observations of ZnO (a); TEM observation of ZnO (b); SEM observations of g-C_3N_4 (c); biochar (d); ZCN (e); ZCN (f), ZCNB (g); and ZCNB (h); and HRTEM observations of ZCNB (i).

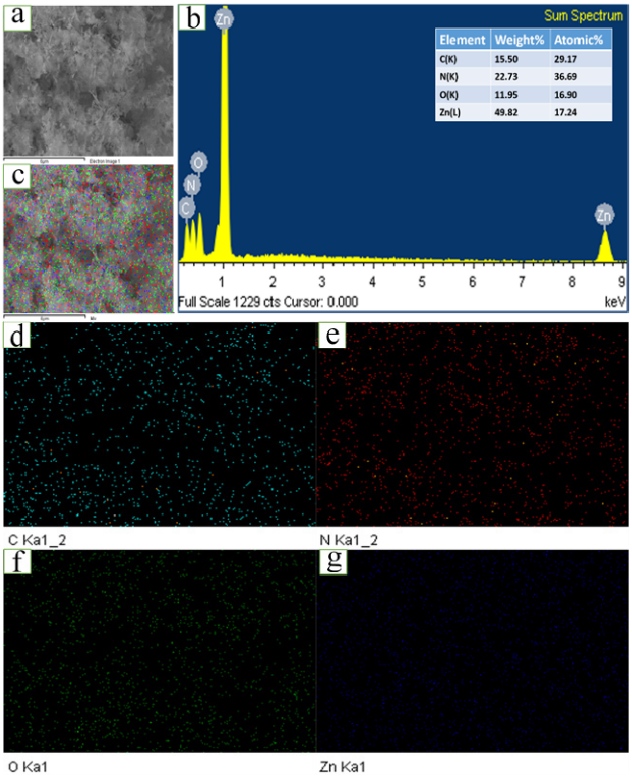

Fig. 3. a) electron image and b) EDX spectrum of ZCNB sample; c) elemental mapping image of C, N, O, and Zn on ZCNB; EDX elemental mapping of d) C, e) N, f) O, and g) Zn.

O 16.9, and Zn 17.24% (the inset of Fig. 3b). These results demonstrate that ZnO nanoparticles are highly dispersed on *g*-C_3N_4 and biochar.

The core-level XPS of Zn 2p, O 1s, C 1s and N 1s of ZCNB are presented in Fig. 4. The Zn 2p spectrum at 1024.7 eV and 1047.8 eV are acribed Zn $2p_{3/2}$ and Zn $2p_{1/2}$ of hexagonal structure (Fig. 4a) [48]. O 1s spectrum of Fig. 4b presents the peaks at 524.5 eV and 526.3 eV contributed to O^{2-} in ZnO, while peaks at 533.5 eV, 534.5 eV and 535.4 eV belong to O^{2-} in oxigen deffect in ZnO or the OH and O2 adsorbed on the catalyst surface, respectively [48, 64]. The presence of O_2 in defected region make it form $O^{2-\cdot}$ and improve catalytic ativity (Fig. 4b) [64]. C 1s spectrum peaks at 281.6 eV, 287.5 eV that assigned to C–N [65] and 290.6 eV corresponding to bonding energy of C in C–$(N)_3$ [66, 67] or C=O [68] (Fig. 4c). The core-level XPS of N 1s is deconvulated into three peaks at 397.2 eV, 399.1 eV and 407.6 eV, which are assigned to the sp^2 hybridized nitrogen C=N–C, tertiary N in N–C_3 and N atoms in amino moieties, respectively (Fig. 4d) [64, 65, 69].

3.2. Photocatalytic Degradation of Doxycycline over ZCNB Catalyst

For primary tests, the effect of the different catalyst loadings (0.05, 0.10, 0.15, and 0.20 grams) in 200 mL of 25 $mg.L^{-1}$ DC at pH 5 on DC degradation is depicted in Fig. S1a. DC decomposition efficiency increased from 90.9 to 99.8% corresponding to an increase in the amount of ZCNB from 0.05 to 0.20 grams. This may be due to the presence of more active sites with increasing ZCNB dosage and thus facilitating the generation of oxidation

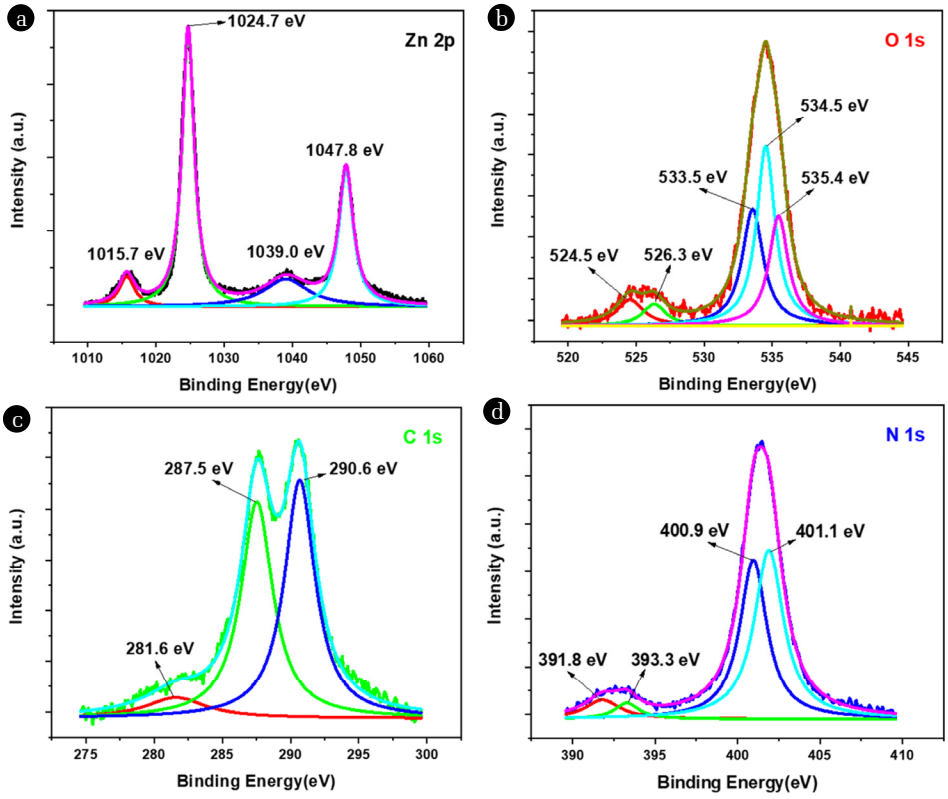

Fig. 4. XPS spectra of ZCNB composite: a) Zn 2p, b) O 1s, c) C 1s, and N 1s.

agents [70]. The sample at the amount of ZCNB 0.10 gram showed a fairly high DC decomposition efficiency (98.9%), and therefore we chose this amount of catalyst as the appropriate condition for the further experiments.

The photocatalytic activity of pristine ZnO, pristine *g*-C_3N_4, ZCN, and ZCNB was studied via doxycycline photodegradation under visible light irradiation ($\lambda > 420$ nm) (Fig. 5a). When no catalysts are applied, no photolysis of DC is observed after 2 h of visible light irradiation, demonstrating that DC is stable under visible light [40, 71]. Similarly, ZnO does not favour DC decomposition under visible light radiation. Like previously reported results [72, 73], pristine *g*-C_3N_4 exhibits good performance in photodegradation under visible light in the present work. The ZCN composite has a much higher photocatalytic activity than pristine *g*-C_3N_4 for DC degradation, with an efficiency of 69.74% after 120 min. Meanwhile, the ZCNB photocatalyst is the most active in DC degradation, with an efficiency of 98.9%.

To better understand the reaction kinetics of DC degradation catalyzed by different photocatalysts, we fitted the experimental data with the Langmuir-Hinshelwood first-order model (Eq. 3). As can be seen from Fig. 5b, the photocatalytic degradation curves in all cases are consistent with the apparent first-order kinetic model with high determination coefficients ($R^2 > 0.95$). Furthermore, a significant difference in the photocatalytic activity of ZCNB from the others implies that the incorporation of ZnO with *g*-C_3N_4 and biochar substantially improves the photocatalytic activity of ZnO, and this composite has the highest degradation rate constant for DC photodegradation. The rate constant for ZnO, *g*-C_3N_4, ZCN, and ZCNB is about 2.39×10^{-4}, 0.007, 0.016, and 0.069 min^{-1}, respectively. The ZCNB composite is about 9.31 and 4.18 times more effective than pristine *g*-C_3N_4 and ZCN. A comparison of the first-order apparent degradation rate constant of the present catalyst with the literature is presented in Table S5. The data show that the catalytic activity of the ZCNB composite is relatively high compared with what was reported in previous papers [6, 39, 72-74].

The COD values were determined to assess the mineralisation of DC over ZCNB (Fig. 5c). It is clear that the COD gradually decreases with time, indicating a gradual decomposition of DC. The reduction of COD up to 93.52% is achieved after 120 min of illumination with the ZCNB composite. Therefore, it can be concluded that the DC is decomposed into carbon dioxide over the ZCNB almost completely.

Since photocatalytic degradation involves photo-induced electron/hole pairs (e^-/h^+), superoxide radicals ($\bullet O_2^-$) and hydroxyl radicals (•OH), several scavengers were used to study the effect of free radicals on DC degradation (Fig. 5d). For these experiments, 10 mM of potassium iodide (KI), potassium bromate ($KBrO_3$), tert-butanol (t-BA), and ascorbic acid (AA) was added to the DC solution to capture h^+, e^-, •OH, and $\bullet O_2^-$, respectively. Fig. 5d shows that the degradation efficiency drops to 33.61, 58.58, 80.14, and 71.88% upon the addition of KI, $KBrO_3$, tBA, and AA,

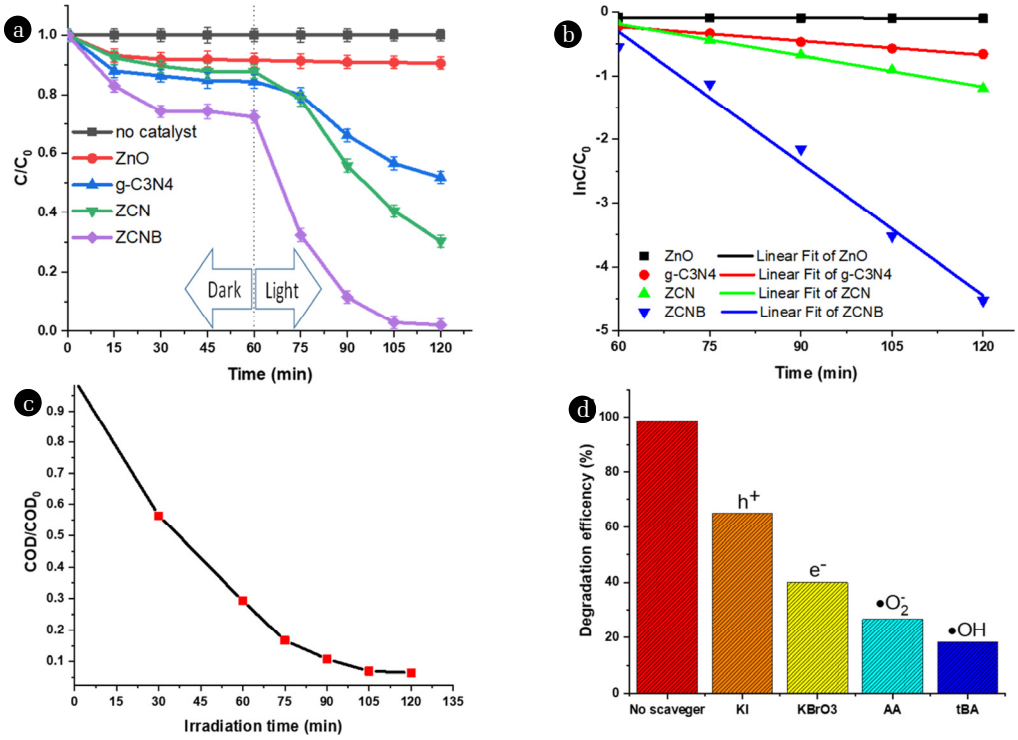

Fig. 5. a) Photodegradation of doxycycline over no catalyst, ZnO, g-C_3N_4, ZCN, and ZCNB. b) First-order kinetics plot for the photodegradation of doxycycline by ZnO, g-C_3N_4, ZCN, and ZCNB samples; c) COD value versus irradiation time; d) Effect of different scavengers on doxycycline photodegradation over ZCNB samples. (Mass of catalyst: 0.1 gram; DC concentration of 25 mg·L^{-1}; the volume of 200 mL (pH~5); time for dark adsorption is 60 min and for illumination is 120 minutes).

respectively. First, tBA is considered a scavenger for •OH [72], it is considered that *t*-BA presents a strong interaction with the •OH through an electron transfer process [75].

$$\text{t-BA} + \bullet\text{OH} \rightarrow \text{t-butanyl–O}\bullet + \text{H}_2\text{O} \quad (5)$$

If the •OH radicals play a crucial role in the DC degradation, the reaction rate is expected to decrease significantly. As shown in Fig. 5d, adding an excess amount of t-BA to the reaction mixture significantly suppresses the DC degradation (by ~ 80.1%) compared with the mixtures without the scavenger. Secondly, the addition of AA drops the decomposition efficiency by around 71.9% compared with the absence of scavenger. Like benzoquinone, AA exhibits ability to capture $\bullet O_2^-$ by an electron transfer mechanism [76],

$$\text{AA} + \bullet O_2^- \rightarrow \bullet \text{AA}^- + O_2 \quad (6)$$

Thirdly, the BrO_3^- ion captures photogenerated electrons and then reduces to bromide (Br^-) [77],

$$BrO_3^- + e_{cb}^- + 6H^+ \rightarrow Br^- + 3H_2O \quad (7)$$

and the addition of the $KBrO_3$ makes the degradation efficiency dropping around 58.58% compared with the absence of scavenger.

Finally, the iodide ion is a common scavenger that reacts with vacancy-band holes [78].

$$h^+ + I^- \rightarrow \bullet I \quad (8)$$

$$\bullet I^+ + I^- \rightarrow \bullet I_2^- \quad (9)$$

$$h^+ + \bullet I_2^- \rightarrow I_2 \quad (10)$$

The addition of the KI reduces the degradation efficiency only to 33.62%. Therefore, it can be concluded that the formation of •OH and $\bullet O_2^-$ play an essential role in the photocatalytic degradation of DC.

The electrons and holes generated in the photocatalyst react with the water and oxygen molecules adsorbed on the catalyst surface and generate •OH and $\bullet O_2^-$ that react to decompose the DC molecules in solutions [44,45].

The valence-band energy potential (E_{VB}) and conduction-band energy potential (E_{CB}) of a semiconductor can be calculated as follows [22]:

$$E_{VB} = \chi - E_e + 0.5 \times E_{bg} \quad (11)$$

$$E_{CB} = E_{VB} - E_{bg} \quad (12)$$

where χ is the absolute electronegativity of the semiconductor, and the values of χ were 4.74 and 5.6 eV for *g*-C_3N_4 and ZnO [22]. E_e is the energy of free electrons versus hydrogen (4.5 eV), and E_{bg} is the bandgap value of the semiconductor. The calculated

values of E_{VB} and E_{CB} are 2.69 and –0.49 eV for ZnO and 1.635 and –1.155 eV for g-C_3N_4. Because of the different positions of valence-band and conduction-band potentials between ZnO and g-C_3N_4, type II heterojunction can occur with coupling effects [79]. The ZnO semiconductor cannot be excited under visible-light illumination since it has a large band gap (3.18 eV). Pristine g-C_3N_4, with its narrow bandgap energy (2.79 eV), is excited by visible light to create photo-generated electron-hole pairs (Eq. 13). Since the CB edge potential (–1.155 eV) of g-C_3N_4 is more negative than that of ZnO (–0.49 eV), the photoinduced electrons in the conduction band of g-C_3N_4 transfer directly to the conduction band of ZnO and subsequently to the surface of ZCNB [80]. On the other hand, biochar on the ZCNB composite surface can also accept electrons on the conduction band of ZnO or g-C_3N_4 [77, 78]. The photosensitive electrons on the catalyst surface react with O_2 dissolved in the solution and create $\bullet O_2^-$ (Eq. 14). These radicals continue to react with adsorbed H_2O on the surface of the catalyst or H^+ ions present in the solution to form •OH (Eq. 15–18), and the resulting •OH decomposes DC [22] (Eq. 19). On the opposite side, since the VB edge potential of ZnO (2.69 eV) is more positive than the potential of the $\bullet OH/OH^-$ pair (1.99 eV) [81], the holes in the valence band cannot react with the OH^- ion to form active •OH, but they can instead directly oxidize DC molecules (Eq. 20 and 21) [23, 82]. Based on the literature [22, 82-84] and the aforementioned results, we propose a possible visible light-driven photocatalytic mechanism at the interface of the ZCNB heterojunction. Briefly, visible light excites g-C_3N_4 to form photoinduced electron/hole pairs. Then these photogenerated electrons transferred directly to the conduction band of ZnO and the surface of ZCNB lead the promotion of separation of photogenerated electron-hole pairs. These free electrons will react with oxygen to form $\bullet O_2^-$, followed by the reactions of these radicals with H_2O or H^+ to form •OH. This process is illustrated as shown in Fig. 6.

$$\text{ZCNB} + h\nu \rightarrow \text{ZCNB}\ (e^- + h^+) \quad (13)$$

$$\text{ZCNB}\ (e^-) + O_2 \rightarrow \text{ZCNB} + \bullet O_2^- \quad (14)$$

$$\bullet O_2^- + H^+ \rightarrow \bullet HO_2 + OH^- \quad (15)$$

$$\bullet O_2^- + H^+ \rightarrow \bullet HO_2 + OH^- \quad (16)$$

$$2\bullet HO_2 \rightarrow H_2O_2 + O_2 \quad (17)$$

$$H_2O_2 + e \rightarrow \bullet OH + OH^- \quad (18)$$

$$\bullet OH + \text{pollutant (DC)} \rightarrow \text{Degradation products} \quad (19)$$

$$\bullet O_2^- + \text{pollutant (DC)} \rightarrow \text{Degradation products} \quad (20)$$

$$h^+ + \text{pollutant (DC)} \rightarrow \text{Degradation products} \quad (21)$$

In addion, we applied ZCNB composites to decompose other types of pollutants under visible light illumination. As presented in Fig. S1b, ZCNB exhibited an excellent degradation efficiency within 120 min for ciprofloxacin (98.2%), amoxicillin (90.3%), methylene blue (95.2%), rhodamine B (99.9%), and methyl orange (82.4%). These results show that composites have great potential for applications in treating organic pollutants in wastewater.

Inorganic anions can trap oxidants that play a prominent role in photocatalysis, reducing the decomposition ability of the photocatalytic treatment system. For this reason, this study incorporated 1.0 mM of ions commonly present in natural waters namely Cl^-, PO_4^{3-}, CO_3^{2-}, NO_3^- and SO_4^{2-} into the reactor (anion/DC molar ratio of 20.5) as coexisting anions to show their impact on the DC degradation rate. The reactions were conducted under selected conditions with a pH of 5.0, a catalyst amount of 0.1 g, and 200 mL of DC solution at a concentration of 25 mg L^{-1}. The results are illustrated in Fig. S1c. It is observed that all these anions have the effect of reducing DC decomposition efficiency. Adsorption of these anions onto the active sites of the catalyst will reduce the available surface sites for DC adsorption, as will

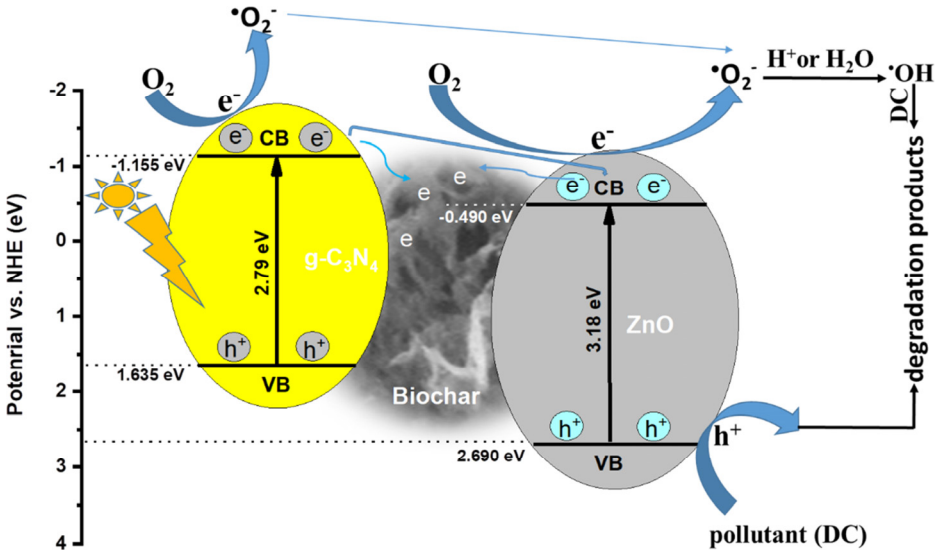

Fig. 6. Schematic representation of the photocatalytic mechanism over composite ZCNB.

the reaction of the anions with oxidizing agents to produce oxygen species less strong oxidation, are the main reasons for the smaller DC removal efficiency in the presence of these anions [85]. Among the combined anions, phosphate and nitrate showed a slight decreasing effect on the degradation rate, reducing the removal efficiency from 98.9 to 90.1 and 93.5%, respectively. In contrast, the addition of carbonate, chloride and sulfate resulted in a significant decrease in DC degradation efficiency to 55.6, 62.5 and 73.9%, respectively. It seems that the stronger competition of carbonate, chloride and sulfate anions with DC for adsorption on the ZCNB surface and the scavenging of oxidative radicals by these ions is responsible for their destructive effects on the ZCNB surface. with effective DC removal [86]. The quenching effect of carbonate, chloride and sulfate anions can be described by equations (22)–(24).

$$CO_3^{2-} + \bullet OH \rightarrow OH^- + \bullet CO_3^- \quad (22)$$

$$Cl^- + \bullet OH \rightarrow OH^- + \bullet Cl \quad (23)$$

$$SO_4^{2-} + \bullet OH \rightarrow OH^- + \bullet SO_4^- \quad (24)$$

3.3. Recyclability and Real Sample Test

For the purposes of practical applications, it is necessary to evaluate the long-term stability of the photocatalyst during the reaction. The ZCNB catalyst was reused four times. After each test, the catalyst was separated by using centrifugation; then, it was eluted several times with methanol [87] to ensure complete removal of residual DC, and finally was dried at 105℃ for 24 h. The photocatalytic degradation efficiency of ZCNB decreases from 98.9 to 90.1% after six cycles (Fig. 7a). The XRD patterns of the ZCNB samples before and after the fourth test remain almost unchanged; therefore, it can be concluded that ZCNB is stable in the photocatalytic degradation reactions (Fig. 7b).

The shrimp aquaculture wastewater was collected from a shrimp aquaculture pool at Mekong delta. The characteristics of shrimp farming wastewater samples are shown in Table S6. It was used to test DC degradation over the present catalyst (Fig. 7c). Around 90% of DC is degraded after 120 minutes. In addition, ZCNB also showed a certain degradation effect on other pollution (Table S6). The TOC and COD removal efficiency reached values of 73.1% and 87.1%, respectively, showing that ZCNB is a promising material in practical wastewater treatment.

4. Conclusions

A tertiary nanocomposite ZnO/g-C_3N_4/biochar was synthesised with the hydrolysis method. The composite consists of ZnO nanoparticles with a size of about 25–30 nm, highly dispersed on the g-C_3N_4 and biochar matrix. The ZnO/g-C_3N_4/biochar composite

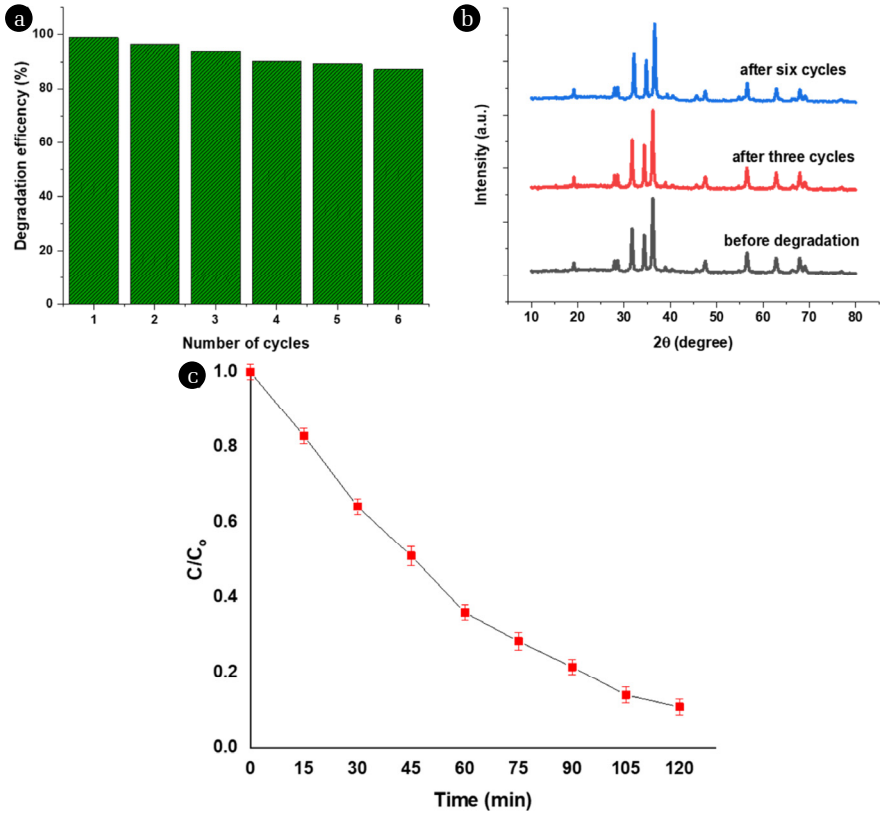

Fig. 7. a) Reusability of the ZCNB nanocomposite in six successive runs; b) XRD patterns of used ZCNB after third and sixth cycle (Mass of catalyst: 0.1 gram; DC concentration of 25 mg·L^{-1}; the volume of 200 mL (pH~5); time for dark adsorption is 60 min and for illumination is 120 minutes) and c) DC degradation in the real shrimp aquaculture wasterwater over ZCNB catalyst.

exhibits a significantly higher photodegradation efficiency for doxycycline than g-C_3N_4 and ZnO under visible light. The catalyst is stable during operation. The present study proposes a premise to obtain an inexpensive photocatalyst from biomass waste. This ZnO/g-C_3N_4/biochar catalyst can be used for the antibiotics photodegradation in aqueous solutions. However, some limitation of this process need acknowledgement including g-C_3N_4 production in anaerobic conditions in large-scale, large volumes of wastewater treatment, the complex wastewater compositions and the difficult recovery of catalysts due to small particle sizes.

Acknowledgements

This research was supported by The Ministry of Education and Training, Vietnam, under the project coded B2022.SPD.562.07.

Conflicts of Interest

The authors declare that they have no conflicts of interest.

Author Contributions

The authors confirm contribution to the paper as follows: N.V.H. (Associate Professor) and D.Q.K. (Professor) study conception, design, draft, and final manuscript preparation; B.T.M.N. (Ph.D.), N.H.N. (Master), N.M.L. (Master) and N.N.B (Ph.D.) data collection; L.V.T.S. (Master); N.T.K. (Ph.D.), Đ.N.N. (Associate Professor) and N.T.T. (PhD student) analysis and interpretation of results. All authors reviewed the results and approved the final version of the manuscript.

References

1. Ahmed MJ. Adsorption of quinolone, tetracycline, and penicillin antibiotics from aqueous solution using activated carbons: Review. *Environ. Toxicol. Pharmacol*. 2017;50:1–10. https://doi.org/10.1016/j.etap.2017.01.004.
2. Wang J, Zhuan R. Degradation of antibiotics by advanced oxidation processes: An overview. *Sci. Total Environ*. 2020;701:135023. https://doi.org/10.1016/j.scitotenv.2019.135023.
3. Liu W, Zhou J, Hu Z. Nano-sized g-C_3N_4 thin layer @CeO_2 sphere core-shell photocatalyst combined with H_2O_2 to degrade doxycycline in water under visible light irradiation. *Sep. Purif. Technol*. 2019;227:115665. https://doi.org/10.1016/j.seppur.2019.06.003.
4. Bolobajev J, Trapido M, Goi A. Effect of iron ion on doxycycline photocatalytic and Fenton-based autocatatalytic decomposition. *Chemosphere*. 2016;153:220–226. https://doi.org/10.1016/j.chemosphere.2016.03.042.
5. Mohammadi A, Pourmoslemi S. Enhanced photocatalytic degradation of doxycycline using a magnetic polymer-ZnO composite. *Water Sci. Technol*. 2018;2017(3):791–801. https://doi.org/10.2166/wst.2018.237.
6. Yan X, Qian J, Pei X et al. Enhanced photodegradation of doxycycline (DOX) in the sustainable $NiFe_2O_4$/MWCNTs/BiOI system under UV light irradiation. *Environ. Res*. 2021;199:111264. https://doi.org/10.1016/j.envres.2021.111264.
7. Ouyang J, Zhou L, Liu Z, Heng JYY, Chen W. Biomass-derived activated carbons for the removal of pharmaceutical mircopollutants from wastewater: A review. *Sep. Purif. Technol*. 2020;253:117536. https://doi.org/10.1016/j.seppur.2020.117536.
8. Cheng S, Chen Q, Xia H et al. Microwave one-pot production of ZnO/Fe_3O_4/activated carbon composite for organic dye removal and the pyrolysis exhaust recycle. *J. Clean. Prod*. 2018;188:900–910. https://doi.org/10.1016/j.jclepro.2018.03.308.
9. Vinayagam M, Ramachandran S, Ramya V, Sivasamy A. Photocatalytic degradation of orange G dye using ZnO/biomass activated carbon nanocomposite. *J. Enviro. Chem. Eng*. 2018;6(3):3726–3734. https://doi.org/10.1016/j.jece.2017.06.005.
10. Khan ZUH, Gul NS, Sabahat S et al. Removal of organic pollutants through hydroxyl radical-based advanced oxidation processes. *Ecotoxicol. Environ. Saf*. 2023;267:115564. https://doi.org/10.1016/j.ecoenv.2023.115564.
11. Okab AA, Jabbar ZH, Graimed BH, Alwared AI, Ammar SH, Hussein MAA. A comprehensive review highlights the photocatalytic heterojunctions and their superiority in the photo-destruction of organic pollutants in industrial wastewater. *Inorg. Chem. Commun*. 2023;158:111503. https://doi.org/10.1016/j. inoche.2023.111503.
12. Pallavolu MR, Maddaka R, Viswanath SK, Banerjee AN, Kim MD, Joo SW. High-responsivity self-powered UV photodetector performance of pristine and V-doped ZnO nano-flowers. *Opt. Laser Techno*. 2023;157:108776. https://doi.org/10.1016/j.optlastec.2022.108776.
13. Han C, Li X, Shao C et al. Composition-controllable p-CuO/n-ZnO hollow nanofibers for high-performance H_2S detection. *Sens. Actuators B: Chem*. 2019;285:495-503. https://doi.org/10.1016/j.snb.2019.01.077.
14. Grau PB, Domene RMF, Tovar RS, Antón JG. Control on the morphology and photoelectrocatalytic properties of ZnO nanostructures by simple anodization varying electrolyte composition. *J. Electro. Chem*. 2021;880:114933. https://doi.org/10.1016/j.jelechem.2020.114933.
15. Devi LR, Sundar SM. Investigation on structural, photoluminescence and magnetic behavior of Mn-ZnO nanoparticles via solvothermal route. *J. Indian Chem. Soc*. 2023;100(7):101036. https://doi.org/10.1016/j.jics.2023.101036.
16. Dymshits O, Gorokhova E, Alekseeva I et al. Transparent materials based on semiconducting ZnO: glass-ceramics and optical ceramics doped with rare-earth and transition-metal ions. *J. Non Cryst. Solids*. 2022;588:121625. https://doi.org/10.1016/j.jnoncrysol.2022.121625.
17. Li Y, Xu R, Qiao L et al. Controlled synthesis of ZnO modified N-doped porous carbon nanofiber membrane for highly efficient removal of heavy metal ions by capacitive deionization. *Micro. Meso. Mater*. 2022;338:111889. https://doi.org/10.1016/j.micromeso.2022.111889.
18. Yılmaz G, Dindar B. Non-metal doped ZnO photocatalyst prepared by sonication-assisted sol-gel method and use for dye

degradation. *Inorg. Chem. Commun*. 2023;157:111320. https://doi.org/10.1016/j.inoche.2023.111320.
19. Sawunyama L, Oyewo O, Onwudiwe DC, Makgato SS. Photocatalytic degradation of tetracycline using surface defective black TiO_2-ZnO heterojunction photocatalyst under visible light. *Heliyon*. 2023;9(11):e21423. https://doi.org/10.1016/j.heliyon.2023.e21423.
20. Wang L, Ma C, Guo Z et al. In-situ growth of g-C_3N_4 layer on ZnO nanoparticles with enhanced photocatalytic performances under visible light irradiation. *Mater. Lett*. 2017;188:347-350. https://doi.org/10.1016/j.matlet.2016.11.113.
21. Chen Q, Hou H, Zhang D et al. Enhanced visible-light driven photocatalytic activity of hybrid ZnO/g-C_3N_4 by high performance ball milling. *J. Photochem. Photobiol. A Chem*. 2018;350:1-9. https://doi.org/10.1016/j.jphotochem.2017.09.015.
22. Prabhu S, Pudukudy M, Harish S et al. Facile construction of djembe-like ZnO and its composite with g-C_3N_4 as a visible-light-driven heterojunction photocatalyst for the degradation of organic dyes. *Mater. Sci. Semicond. Process*. 2020;106:104754. https://doi.org/10.1016/j.mssp.2019.104754.
23. Kuang PY, Su YZ, Chen GF et al. g-C_3N_4 decorated ZnO nanorod arrays for enhanced photoelectrocatalytic performance. *Appl. Surf. Sci*. 2015;358:296-303. https://doi.org/10.1016/j.apsusc.2015.08.066.
24. Nag I. Development of an engineered face mask with optimized nanoparticle layering for filtration of air pollutants and viral pathogens. *Environ. Eng. Res*. 2023;28(6):230003. https://doi.org/10.4491/eer.2023.003.
25. Stiadi Y, Wendari TP, Zilfa, Zulhadjri, Rahmayeni. Tuning the structural, magnetic, and optical properties of ZnO/$NiFe_2O_4$ heterojunction photocatalyst for simultaneous photodegradation of Rhodamine B and Methylene Blue under natural sunlight. *Environ. Eng. Res.* 2022;28(3):220074. https://doi.org/10.4491/eer.2022.074.
26. Shokrollahzadeh S, Abassi M, Ranjbar M. A new nano-ZnO/perlite as an efficient catalyst for catalytic ozonation of azo dye. *Environ. Eng. Res.* 2019;24(3):513-520. https://doi.org/10.4491/eer.2018.322.
27. Ravichandran K, Kalpana K, Uma R, Sindhuja E, Seelan KS. Cost-effective fabrication of ZnO/g-C_3N_4 composite film coated stainless steel meshes for visible light responsive photocatalysis. *Mater. Res. Bulletin*. 2018;99:268-280. https://doi.org/10.1016/j.materresbull.2017.11.010.
28. Škuta R, Kostura B, Ritz M, Foniok K, Pavlovský J, Matýsek D. Comparing the photocatalytic performance of GO/ZnO and g-C_3N_4/ZnO composites prepared using metallurgical waste as a source of zinc. *Inorg. Chem. Commun*. 2023;152:110728. https://doi.org/10.1016/j.inoche.2023.110728.
29. Xiao Y, Lyu H, Yang C, Zhao B, Wang L, Tang J. Graphitic carbon nitride/biochar composite synthesized by a facile ball-milling method for the adsorption and photocatalytic degradation of enrofloxacin. *J. Environ. Sci*. 2021;103:93-107. https://doi.org/10.1016/j.jes.2020.10.006.
30. Zheng Y, Yang Y, Zhang Y et al. Facile one-step synthesis of graphitic carbon nitride-modified biochar for the removal of reactive red 120 through adsorption and photocatalytic degradation. *Biochar*. 2019;1(1):89-96. https://doi.org/10.1007/s42773-019-00007-4.
31. Guo J, Jiang S, Lin Z et al. Pyrolysis of torrefied Phragmites australis from atmospheric and gas-pressurized torrefaction: Pyrolysis kinetic and product analysis. *J. Anal. Appl. Pyrolysis*. 2022;167:105670. https://doi.org/10.1016/j.jaap.2022.105670.
32. Sousa JGMD, Silva TVCD, Moraes NPD et al. Visible light-driven ZnO/g-C_3N_4/carbon xerogel ternary photocatalyst with enhanced activity for 4-chlorophenol degradation. *Mater. Chem. Phys*. 2020;256:123651. https://doi.org/10.1016/j.matchemphys.2020.123651.
33. Guan K, Zhou P, Zhang J, Zhu L. Synthesis and characterization of ZnO@RSDBC composites and their Photo-Oxidative degradation of Acid Orange 7 in water. *J. Mol. Structure*. 2020;203:127425. https://doi.org/10.1016/j.molstruc.2019.127425.
34. Zhai S, Li M, Wang D, Zhang L, Yang Y, Fu S. In situ loading metal oxide particles on bio-chars: Reusable materials for efficient removal of methylene blue from wastewater. *J. Clean. Prod.* 2019;220:460-474. https://doi.org/10.1016/j.jclepro.2019.02.152.
35. Chen XL, Li F, Zhang M, Liu B, Chen H, Wang H. Highly dispersed and stabilized Co_3O_4/C anchored on porous biochar for bisphenol A degradation by sulfate radical advanced oxidation process. *Sci. Total Environ.* 2021;777:145794. https://doi.org/10.1016/j.scitotenv.2021.145794.
36. Wei X, Wang X, Gao B, Zou W, Dong L. Facile ball-milling synthesis of CuO/Biochar nanocomposites for efficient removal of Reactive Red 120. *ACS Omega*. 2020;5(11):5748-5755. https://doi.org/10.1021/acsomega.9b03787.
37. Geng A, Xu L, Gan L et al. Using wood flour waste to produce biochar as the support to enhance the visible-light photocatalytic performance of BiOBr for organic and inorganic contaminants removal. *Chemosphere.* 2020;250:126291. https://doi.org/10.1016/j.chemosphere.2020.126291.
38. Nguyet BTM, Nghi NH, Tien NA, Khieu DQ, Duc HD, Hung NV. Enhanced adsorption of methylene blue by chemically modified materials derived from *Phragmites australis* stems. *Acta. Chim. Slov.* 2022;69(4):7567. https://doi.org/10.17344/acsi.2022.7567.
.39.Liu W, Zhang J, Kang Q, Chen H, Feng R. Enhanced photocatalytic degradation performance of In_2O_3/g-C_3N_4 composites by coupling with H_2O_2. *Ecotoxicol. Environ. Saf.* 2023;252:114611. https://doi.org/10.1016/j.ecoenv.2023.114611.
40. Liu J, Zhou S, Gu P et al. Conjugate Polymer-clothed TiO_2@V_2O_5 nanobelts and their enhanced visible light photocatalytic performance in water remediation. *J. Colloid Interface Sci*. 2020;578:402–411. https://doi.org/10.1016/j.jcis.2020.06.014.
41. Raizada P, Singh P, Kumar A et al. Solar photocatalytic activity of nano-ZnO supported on activated carbon or brick grain particles: Role of adsorption in dye degradation. *Appl. Catal. A-Gen.* 2014;486:159–169. https://doi.org/10.1016/j.apcata.2014.08.043.
42. He Y, Wang Y, Hu J et al. Photocatalytic property correlated with microstructural evolution of the biochar/ZnO composites. *J. Mater. Res. Technol*. 2021;11:1308–1321. https://doi.org/10.1016/j.jmrt.2021.01.077.
43. Djoko SYT, Bashiri H, Njoyim ET et al. Urea and green tea like precursors for the preparation of g-C_3N_4 based carbon nanomaterials (CNMs) composites as photocatalysts for photodegradation of pollutants under UV light irradiation. *J.*

Photochem. Photobiol. A: Chem. 2020;398:112596. https://doi.org/10.1016/j.jphotochem.2020.112596.
44. Huang L, Liu H, Wang Y, Zhang TC, Yuan S. Construction of ternary Bi_2O_3/biochar/g-C_3N_4 heterojunction to accelerate photoinduced carrier separation for enhanced tetracycline photodegradation. *Appl. Surf. Sci*. 2023;616:156509. https://doi.org/10.1016/j.apsusc.2023.156509.
45. Li Y, Liu Z, Li Z, Wang Q. Renewable biomass-derived carbon-supported g-C_3N_4 doped with Ag for enhanced photocatalytic reduction of CO_2. *J. Colloid Interface Sci*. 2022;606 (Pt2):1311-1321. https://doi.org/10.1016/j.jcis.2021.08.176.
46. Martins NDJ, Gomes ICH, Silva GTSTD et al. Facile preparation of ZnO:g-C_3N_4 heterostructures and their application in amiloride photodegradation and CO_2 photoreduction. *J. Alloys Compd*. 2021;856:156798. https://doi.org/10.1016/j.jallcom.2020.156798.
47. Zhang W, Yin J, Chen C, Qiu X. Carbon nitride derived nitrogen-doped carbon nanosheets for high-rate lithium-ion storage. *Chem. Eng. Sci*. 2021;241:116709. https://doi.org/10.1016/j.ces.2021.116709.
48. Zhong Q, Lan H, Zhang M, Zhu H, Bu M. Preparation of heterostructure g-C_3N_4/ZnO nanorods for high photocatalytic activity on different pollutants (MB, RhB, Cr(VI) and eosin). *Ceram. Int*. 2020;46(8):12192-12199. https://doi.org/10.1016/j.ceramint.2020.01.265.
49. Liang S, Sui G, Guo D et al. g-C_3N_4-wrapped nickel doped zinc oxide/carbon core-double shell microspheres for high-performance photocatalytic hydrogen production. *J. Colloid Interface Sci*. 2023;635:83-93. https://doi.org/10.1016/j.jcis.2022.12.120.
50. Hu H, Sun L, Gao Y et al. Synthesis of ZnO nanoparticle-anchored biochar composites for the selective removal of perrhenate, a surrogate for pertechnetate, from radioactive effluents. *J. Hazard. Mater*. 2020;387:121670. https://doi.org/10.1016/j.jhazmat.2019.121670.
51. Li Y, Liu X. Activated carbon/ZnO composites prepared using hydrochars as intermediate and their electrochemical performance in supercapacitor. *Mater. Chem. Phys*. 2014;148(1–2):380–386. https://doi.org/10.1016/j.matchemphys.2014.07.058.
52. Jafari M, Rahimi MR, Ghaedi M, Javadian H, Asfaram A. Fixed-bed column performances of azure-II and auramine-O adsorption by Pinus eldarica stalks activated carbon and its composite with zno nanoparticles: Optimization by response surface methodology based on central composite design. *J. Colloid Interface Sci*. 2017;507:172–189. https://doi.org/10.1016/j.jcis.2017.07.056.
53. Gholami P, Dinpazhoh L, Khataee A, Orooji Y. Sonocatalytic activity of biochar-supported ZnO nanorods in degradation of gemifloxacin: Synergy study, effect of parameters and phytotoxicity evaluation. *Ultra. Sonochem*. 2019;55:44-56. https://doi.org/10.1016/j.ultsonch.2019.03.001.
54. Xie Y, Zhuo Y, Liu S et al. Ternary g-C_3N_4/ZnNCN@ZIF-8 hybrid photocatalysts with robust interfacial interactions and enhanced CO_2 reduction performance. *Sol. RRL*. 2020;4(8):1–12. https://doi.org/10.1002/solr.201900440.
55. Wang S, Zhou Y, Han S et al. Carboxymethyl cellulose stabilized ZnO/biochar nanocomposites: Enhanced adsorption and inhibited photocatalytic degradation of methylene blue. *Chemosphere*. 2018;197:20-25. https://doi.org/10.1016/j.chemosphere.2018.01.022.
56. Chand P, Gaur A, Kumar A. Structural and optical properties of ZnO nanoparticles synthesized at different pH values. *J. Alloys Compd*. 2012;539:174-178. https://doi.org/10.1016/j.jallcom.2012.05.104.
57. Guan R, Li J, Zhang J et al. Photocatalytic Performance and Mechanistic Research of ZnO/g-C_3N_4 on degradation of methyl orange. *ACS Omega*. 2019;4(24):20742-20747. https://doi.org/10.1021/acsomega.9b03129.
58. Peng X, Wang M, Dai H, Qiu F, Hu F. In situ growth of carbon nitride on titanium dioxide/hemp stem biochar toward 2D heterostructured photocatalysts for highly photocatalytic activity. *Environ. Sci. Pollut. Res*. 2020;27(31):39198-39210. https://doi.org/10.1007/s11356-020-09381-0.
59. Tautua BMA, Fakayode OJ, Songca SP, Oluwafemi OS. Effect of synthetic conditions on the crystallinity, porosity and magnetic properties of gluconic acid capped iron oxide nanoparticles. *Nano Struct. Nano Obj*. 2020;23:100480. https://doi.org/10.1016/j.nanoso.2020.100480.
60. Hong S, Bruyn KD, Bescher E, Ramseyer C, Kang THK. Porosimetric features of calcium sulfoaluminate and Portland cement pastes: testing protocols and data analysis. *J. Struct. Int. Maint*. 2018;3(1):52-66. https://doi.org/10.1080/24705314.2018.1426168.
61. Zhang H, Su T, Yu S et al. Fabrication of Anderson-Polyoxometalates/TiO_2/C_3N_4 heterojunction composite for efficient visible-light-driven photooxidative desulfurization. *Mol. Catal*. 2023;536:112916. https://doi.org/10.1016/j.mcat.2023.112916.
62. Fernandez LM, Villalba LSG, Milošević O, Rabanal ME. Influence of nanoscale defects on the improvement of photocatalytic activity of Ag/ZnO. *Mater. Charact*. 2022;185:111718. https://doi.org/10.1016/j.matchar.2021.111718.
63. Alsulmi A, Mohammed NN, Soltan A, Messih MFA, Ahmed MA. Engineering S-scheme CuO/ZnO heterojunctions sonochemically for eradicating RhB dye from wastewater under solar radiation. *RSC Adv*. 2023;13(19):13269-13281. https://doi.org/10.1039/D3RA00924F.
64. Gupta B, Gupta AK, Tiwary CS, Ghosal PS. A multivariate modeling and experimental realization of photocatalytic system of engineered S-C_3N_4/ZnO hybrid for ciprofloxacin removal: Influencing factors and degradation pathways. *Environ. Res.* 2020;110390. https://doi.org/10.1016/j.envres.2020.110390.
65. Guo F, Shi W, Guan W, Huang H, Liu Y. Carbon dots/g-C_3N_4/ZnO nanocomposite as efficient visible-light driven photocatalyst for tetracycline total degradation. *Sep. Purif. Technol*. 2017;173:295-303. https://doi.org/10.1016/j.seppur.2016.09.040.
66. Li X, Li M, Yang J et al. Synergistic effect of efficient adsorption g-C_3N_4/ZnO composite for photocatalytic property. *J. Phys. Chem. Solids*. 2014;75(3):441-446. https://doi.org/10.1016/j.jpcs.2013.12.001.
67. Das D, Nandi P. ZnO/g-C_3N_4 heterostructures: Synthesis, characterization and application as photoanode in dye sensitized solar cells. *Sol. Energy Mater. Sol. Cells*. 2022;248:112002. https://doi.org/10.1016/j.solmat.2022.112002.
68. Jung H, Pham TT, Shin EW. Interactions between ZnO nanoparticles and amorphous g-C_3N_4 nanosheets in thermal formation of g-C_3N_4/ZnO composite materials: The annealing tem-

perature effect. *Appl. Surf. Sci*. 2018;458:369-381. https://doi.org/10.1016/j.apsusc.2018.07.048.
69. Nie N, Zhang L, Fu J, Cheng B, Yu J. Self-assembled hierarchical direct Z-scheme g-C_3N_4/ZnO microspheres with enhanced photocatalytic CO_2 reduction performance. *Appl. Surf. Sci*. 2018; 441:12-22. https://doi.org/10.1016/j.apsusc.2018.01.193.
70. Thi NT, Nam SN. Sunlight-driven photocatalysis of dissolved organic matter: Tracking by excitation emission matrix-parallel factor analysis and optimization using response surface methodology. *Environ. Eng. Res*. 2021;26(3):200201. https://doi.org/10.4491/eer.2020.201.
71. Berdini F, Otalvaro JO, Avena M, Brigante M. Photodegradation of doxycycline in water induced by TiO_2-MCM-41. Kinetics, TOC evolution and reusability. *Results Eng*. 2022;16:100765. https://doi.org/10.1016/j.rineng.2022.100765.
72. Swetha S, Maksoud MAA, Okla MK et al. Triple-mechanism driven Fe-doped n-n hetero-architecture of Pr_6O_{11}-MoO_3 decorated g-C_3N_4 for doxycycline degradation and bacterial photoinactivation. *Chem. Eng. J*. 2023;461:141806. https://doi.org/10.1016/j.cej.2023.141806.
73. Dhiman P, Rana G, Alshgari RA et al. Magnetic Ni-Zn ferrite anchored on g-C_3N_4 as nano-photocatalyst for efficient photo-degradation of doxycycline from water. *Environ. Res.* 2023; 216(Pt3):114665. https://doi.org/10.1016/j.envres.2022.114665.
74. Wen Q, Li D, Li H et al. Synergetic effect of photocatalysis and peroxymonosulfate activated by Co/Mn-MOF-74@g-C_3N_4 Z-scheme photocatalyst for removal of tetracycline hydrochloride. *Sep. Purif. Technol*. 2023;313:123518. https://doi.org/10.1016/j.seppur.2023.123518.
75. Buxton GV, Greenstock CL, Helman WP, Ross AB. Critical Review of rate constants for reactions of hydrated electrons, hydrogen atoms and hydroxyl radicals ($\cdot OH/\cdot O^-$ in aqueous solution. *J. Phys. Chem. Ref. Data.* 1988;17(2):513-886. https://doi.org/10.1063/1.555805.
76. Palominos R, Freer J, Mondaca MA, Mansilla HD. Evidence for hole participation during the photocatalytic oxidation of the antibiotic flumequine. *J. Photochem. Photobiol. A Chem*. 2008;193(2-3):139-145. https://doi.org/10.1016/j.jphotochem.2007.06.017.
77. Oosawa Y, Grätzel M. Effect of surface hydroxyl density on photocatalytic oxygen generation in aqueous TiO_2 suspensions. *J. Chem. Soc., Faraday Trans. 1*. 1988;84(1):197-205. https://doi.org/10.1039/F19888400197.
78. Li Y, Wang J, Yao H, Dang L, Li Z. Efficient decomposition of organic compounds and reaction mechanism with BiOI photocatalyst under visible light irradiation. *J. Mol. Catal. A: Chem*. 2011;334(1-2):116-122. https://doi.org/10.1016/j.molcata.2010.11.005.
79. Shi YC, Chen SS, Feng JJ, Lin XX, Wang W, Wang AJ. Dicationic ionic liquid mediated fabrication of Au@Pt nanoparticles supported on reduced graphene oxide with highly catalytic activity for oxygen reduction and hydrogen evolution. *Appl. Surf. Sci*. 2018;441:438–447. https://doi.org/10.1016/j.apsusc.2018.01.240.
80. Qamar MA, Shahid S, Javed M. Synthesis of dynamic g-C_3N_4/Fe@ZnO nanocomposites for environmental remediation applications. *Ceram. Int.* 2020;46(14):22171-22180. https://doi.org/10.1016/j.ceramint.2020.05.294.
81. Mengting Z, Duan L, Zhao Y et al. Fabrication, characterization, and application of BiOI@ZIF-8 nanocomposite for enhanced photocatalytic degradation of acetaminophen from aqueous solutions under UV-vis irradiation. *J. Environ. Manage*. 2023; 345:118772. https://doi.org/10.1016/j.jenvman.2023.118772.
82. Lv H, Ji G, Yang Z et al. Enhancement photocatalytic activity of the graphite-like C_3N_4 coated hollow pencil-like ZnO. *J. Colloid Interface Sci*. 2015;450:381–387. https://doi.org/10.1016/j.jcis.2015.03.038.
83. Liu W, Wang M, Xu C, Chen S. Facile synthesis of g-C_3N_4/ZnO composite with enhanced visible light photooxidation and photoreduction properties. *Chem. Eng. J*. 2012;209:386–393. https://doi.org/10.1016/j.cej.2012.08.033.
84. Mousavi M, Habibi-Yangjeh A. Magnetically separable ternary g-C_3N_4/Fe_3O_4/BiOI nanocomposites: Novel visible-light-driven photocatalysts based on graphitic carbon nitride. *J. Colloid Interface Sci.* 2016;465:83–92. https://doi.org/10.1016/j.jcis.2015.11.057.
85. Payan A, Akbar IA, Gholizade N. Catalytic decomposition of sulfamethazine antibiotic and pharmaceutical wastewater using Cu-TiO_2@functionalized SWCNT ternary porous nanocomposite: Influential factors, mechanism, and pathway studies. *Chem. Eng. J*. 2019;361:1121-1141. https://doi.org/10.1016/j.cej.2018.12.118.
86. Shao B, Liu X, Liu Z et al. A novel double Z-scheme photocatalyst Ag_3PO_4/Bi_2S_3/Bi_2O_3 with enhanced visible-light photocatalytic performance for antibiotic degradation. *Chem. Eng. J*. 2019;368:730-745. https://doi.org/10.1016/j.cej.2019.03.013.
87. He C, Ma J, Xu H, Ge C, Lian Z. Selective capture and determination of doxycycline in marine sediments by using magnetic imprinting dispersive solid-phase extraction coupled with high performance liquid chromatography. *Mar. Pollut. Bull*. 2022; 184:14215. https://doi.org/10.1016/j.marpolbul.2022.114215.